Hydroxo-Bridged Cubane-Type Tetrairon(II) Clusters Supported by Sterically-Hindered Carboxylate Ligands

Dongwhan Lee,† Lorenzo Sorace,‡ Andrea Caneschi,‡ and Stephen J. Lippard*,†

Department of Chemistry, Massachusetts Institute of Technology, Cambridge, Massachusetts 02139, and Department of Chemistry, University of Florence, Via Maragliano 77, I-50144 Firenze, Italy

Received July 9, 2001

A series of hydroxo-bridged cubane-type tetrairon(II) clusters, $[Fe_4(\mu\text{-}OH)_4(\mu\text{-}O_2CAr^{4\text{-}^tBuPh})_2(\mu\text{-}OTf)_2L_4]$ (L = C_5H_5N (**1**), 4-$^tBuC_5H_4N$ (**2**), 3-FC_5H_4N (**3**)), were synthesized by using a sterically hindered carboxylate ligand, 2,6-di(4-*tert*-butylphenyl)benzoate ($Ar^{4\text{-}^tBuPh}CO_2^-$). Three different bridging units that mediate weak antiferromagnetic coupling interactions between the metal centers support the unprecedented cubane-type $\{Fe_4(\mu\text{-}OH)_4\}^{4+}$ cores in **1**−**3**. The solution structures of **1** and **3** probed by FT-IR and ^{19}F NMR spectroscopy are consistent with the solid-state geometry determined by X-ray crystallography. Zero-field Mössbauer spectra of **1**−**3** at 4.2 K are characteristic of high-spin iron(II) centers in nearly identical coordination environments. Compound **1** undergoes two irreversible oxidation processes at ca −10 and +880 mV (vs Fc/Fc^+), the former approaching quasi-reversible behavior with increased scan rates and a narrow potential sweep range. Comparisons are made with analogous known $\{Fe_4X_4\}^{n+}$ (X = O, S) units, and the structural integrity of tetrairon fragments upon a change in oxidation state is discussed together with some possible biological implications.

Introduction

Multiple metal ions connected by single-atom bridging ligands are encountered in proteins participating in electron-transfer (ET) reactions.[1−3] Maintaining efficient shuttling of electrons while minimizing unwanted redox reactions is a delicate task achieved in living systems, the understanding of which has been a topic of extensive research.[3,4] For example, cubane-type $\{Fe_4S_4\}^{n+}$ clusters occur at the active sites of high-potential iron protein (HiPIP; $n = 2/3$ redox couple) or ferredoxin (Fd; $n = 1/2$ redox couple) electron transferases, and these centers have been the subjects of extensive bioinorganic modeling studies.[5−8] Synthetic tetrairon complexes have served as benchmarks for assisting the investigation of their biological counterparts.[5,8] Insights into the electronic structure of biological clusters at various oxidation states have been gleaned from comparison with their low molecular weight analogues having comparable geometric and spectroscopic properties.[2−4]

In contrast to the rich chemistry of $\{Fe_4S_4L_4\}^{n+}$ clusters assembled with a variety of ligand combinations, however, topologically related compounds having oxo or hydroxo bridging groups remain unexplored. Considering the ubiquitous nature of oxo- or hydroxo-bridged iron centers in living systems,[9−11] the participation of analogous $\{Fe_4O_4\}^{n+}$ or $\{Fe_4(OH)_4\}^{n+}$ units in biological ET reactions remains an open question.[12] There are only a few iron alkoxide/phenoxide cubes in which the $\{Fe_4(OR)_4\}^{n+}$ cores are supported by terminal bidentate ligands or bridging carboxylate groups.[13−15] A $\{Fe_4O_4\}^{4+}$ cuboidal fragment was recently identified within a larger octanuclear cluster.[12] Discrete tetrairon clusters having $\{Fe_4(OH)_4\}^{n+}$ or $\{Fe_4O_4\}^{n+}$ cores, however, are unknown in inorganic chemistry.

Recently, we[16−19] and others[20,21] have employed *m*-terphenyl-derived carboxylate ligands[22,23] to model features of non-heme diiron enzyme active sites.[24−26] Site isolation of kinetically labile metal centers within a sterically hindered framework allowed

† Massachusetts Institute of Technology.
‡ University of Florence.

(1) Holm, R. H.; Kennepohl, P.; Solomon, E. I. *Chem. Rev.* **1996**, *96*, 2239−2314.
(2) Solomon, E. I.; Hanson, M. A. In *Inorganic Electronic Structure and Spectroscopy*; Solomon, E. I., Lever, A. B. P., Eds.; John Wiley & Sons: New York, 1999; Vol. II, pp 1−129.
(3) Solomon, E. I.; Randall, D. W.; Glaser, T. *Coord. Chem. Rev.* **2000**, *200*−*202*, 595−632.
(4) Glaser, T.; Hedman, B.; Hodgson, K. O.; Solomon, E. I. *Acc. Chem. Res.* **2000**, *33*, 859−868.
(5) Holm, R. H.; Ciurli, S.; Weigel, J. A. In *Progress in Inorganic Chemistry*; Lippard, S. J., Ed.; John Wiley & Sons: New York, 1990; Vol. 38, pp 1−74.
(6) Lippard, S. J.; Berg, J. M. *Principles of Bioinorganic Chemistry*; University Science Books: Mill Valley, CA, 1994.
(7) Stiefel, E. I.; George, G. N. In *Bioinorganic Chemistry*; Bertini, I., Gray, H. B., Lippard, S. J., Valentine, J. S., Eds.; University Science Books: Mill Valley, CA, 1994.
(8) Beinert, H.; Holm, R. H.; Münck, E. *Science* **1997**, *277*, 653−659.
(9) Lippard, S. J. *Angew. Chem., Int. Ed. Engl.* **1988**, *27*, 344−361.
(10) Kurtz, D. M., Jr. *Chem. Rev.* **1990**, *90*, 585−606.
(11) Powell, A. K. *Struct. Bonding (Berlin)* **1997**, *88*, 1−38.
(12) Raptis, R. G.; Georgakaki, I. P.; Hockless, D. C. R. *Angew. Chem., Int. Ed. Engl.* **1999**, *38*, 1632−1634.
(13) Shoner, S. C.; Power, P. P. *Inorg. Chem.* **1992**, *31*, 1001−1010.
(14) Taft, K. L.; Caneschi, A.; Pence, L. E.; Delfs, C. D.; Papaefthymiou, G. C.; Lippard, S. J. *J. Am. Chem. Soc.* **1993**, *115*, 11753−11766.
(15) Oshio, H.; Hoshino, N.; Ito, T. *J. Am. Chem. Soc.* **2000**, *122*, 12602−12603.
(16) Lee, D.; Lippard, S. J. *J. Am. Chem. Soc.* **1998**, *120*, 12153−12154.
(17) Lee, D.; Du Bois, J.; Petasis, D.; Hendrich, M. P.; Krebs, C.; Huynh, B. H.; Lippard, S. J. *J. Am. Chem. Soc.* **1999**, *121*, 9893−9894.
(18) Lee, D.; Krebs, C.; Huynh, B. H.; Hendrich, M. P.; Lippard, S. J. *J. Am. Chem. Soc.* **2000**, *122*, 5000−5001.
(19) Lee, D.; Lippard, S. J. *J. Am. Chem. Soc.* **2001**, *123*, 4611−4612.
(20) Hagadorn, J. R.; Que, L., Jr.; Tolman, W. B. *J. Am. Chem. Soc.* **1998**, *120*, 13531−13532.
(21) Hagadorn, J. R.; Que, L., Jr.; Tolman, W. B.; Prisecaru, I.; Münck, E. *J. Am. Chem. Soc.* **1999**, *121*, 9760−9761.
(22) Vinod, T. K.; Hart, H. In *Topics in Current Chemistry*; Weber, E., Ed.; Springer-Verlag: Berlin, 1994; Vol. 172, pp 119−178.
(23) Chen, C.-T.; Siegel, J. S. *J. Am. Chem. Soc.* **1994**, *116*, 5959−5960.
(24) Du Bois, J.; Mizoguchi, T. J.; Lippard, S. J. *Coord. Chem. Rev.* **2000**, *200*−*202*, 443−485.
(25) Westerheide, L.; Pascaly, M.; Krebs, B. *Curr. Opin. Chem. Biol.* **2000**, *4*, 235−241.

10.1021/ic010726b CCC: $20.00
Published on Web 11/16/2001

access to dinuclear complexes having unprecedented structures and reactivities. The initial success of this approach prompted us to synthesize a bulkier derivative of this versatile ligand and to investigate the effect of the enhanced steric hindrance on the nuclearity and coordination geometry of the resulting complexes. Installing larger alkyl groups on the 4-positions of the flanking aryl substituents on the benzoate moiety should result in a lateral expansion of the *m*-terphenyl unit, which would translate into restricted access to the metal ions buried inside a sterically more encumbered V-shaped cavity.

In this paper, we describe the synthesis and characterization of a new family of tetrairon(II) clusters. The unprecedented $\{Fe_4(\mu\text{-}OH)_4\}^{4+}$ core is supported by the sterically hindered carboxylate ligand 2,6-di(4-*tert*-butylphenyl)benzoate ($Ar^{4\text{-}tBuPh}CO_2^-$). Unique structural and physical properties of the compounds $[Fe_4(\mu\text{-}OH)_4(\mu\text{-}O_2CAr^{4\text{-}tBuPh})_2(\mu\text{-}OTf)_2L_4]$ (L = C_5H_5N (**1**), 4-^{t}BuC_5H_4N (**2**), 3-FC_5H_4N (**3**)) are described. Comparisons are made with compounds having analogous $\{Fe_4X_4\}^{n+}$ (X = O, S) core fragments, and the structural integrity of tetrairon fragments upon a change in the oxidation state and the biological implications are discussed.

Experimental Section

General Considerations. All reagents were obtained from commercial suppliers and used as received unless otherwise noted. Dichloromethane was distilled over CaH_2 under nitrogen. Diethyl ether, pentanes, and THF were saturated with nitrogen and purified by passage through activated Al_2O_3 columns under nitrogen.[27] $Fe(OTf)_2$·2MeCN was prepared according to literature procedures.[28] All syntheses and air-sensitive manipulations were carried out under nitrogen in a Vacuum Atmospheres drybox or by standard Schlenk line techniques.

Physical Measurements. ^{1}H NMR and ^{19}F NMR spectra were recorded on Varian Mercury 300 MHz and Inova 500 MHz spectrometers, respectively. The chemical shifts of the ^{1}H NMR spectra are reported versus tetramethylsilane and referenced to the residual solvent peaks. ^{19}F chemical shifts are reported with reference to external $CFCl_3$ (0.0 ppm). FT-IR spectra were recorded on a Bio Rad FTS-135 instrument with Win-IR software. Solid samples were pressed into KBr pellets; solution samples were prepared in an airtight Graseby-Specac solution cell with CaF_2 windows. UV−vis spectra were recorded on a Hewlett-Packard 8453 diode array spectrophotometer.

2,6-Di(4-*tert*-butylphenyl)benzoic Acid ($Ar^{4\text{-}tBuPh}CO_2H$). This compound was prepared by a procedure analogous to that used to synthesize $Ar^{Tol}CO_2H$,[29,30] where Ar^{Tol} is 2,6-di(*p*-tolyl)phenyl, except that 1-bromo-4-*tert*-butylbenzene was used instead of 4-bromotoluene. Off-white solid material was obtained by recrystallization from hot hexanes/EtOAc (33% purification yield). Mp: 188 °C. ^{1}H NMR (300 MHz, CD_2Cl_2, 20 °C): δ 7.53 (s, 1H), 7.45−7.34 (m, 10H), 1.36 (s, 18H). ^{13}C NMR (75.47 MHz, CD_2Cl_2, 20 °C): δ 172.9, 151.3, 140.7, 137.9, 131.8, 130.2, 129.5, 128.6, 125.9, 35.0, 31.6. FT-IR (thin film deposited from CD_2Cl_2 solution on NaCl, cm^{-1}): 3029, 2963, 2904, 2868, 2654, 2553, 1699, 1587, 1513, 1460, 1393, 1363, 1296, 1272, 1136, 1118, 1101, 1018, 954, 838, 807, 780, 750, 712, 679, 593, 575. Anal. Calcd for $C_{27}H_{30}O_2$: C, 83.90; H, 7.82. Found: C, 83.99; H, 7.94. The sodium salt of this compound, $NaO_2CAr^{4\text{-}tBuPh}$, was prepared by treating a MeOH solution of the free acid with 1 equiv of NaOH and removing the volatile fractions under reduced pressure.

$[Fe_4(\mu\text{-}OH)_4(\mu\text{-}O_2CAr^{4\text{-}tBuPh})_2(\mu\text{-}OTf)_2(C_5H_5N)_4]$ (1). To a rapidly stirred THF (10 mL) solution of $Fe(OTf)_2$·2MeCN (435 mg, 0.998 mmol) was added $NaO_2CAr^{4\text{-}tBuPh}$ (209 mg, 0.512 mmol). A portion of pyridine (79 mg, 1.0 mmol) was added, and the resulting yellow solution was treated with Et_3N (100 mg, 0.988 mmol). The homogeneous mixture was stirred at room temperature for 0.5 h and treated with Ar-saturated H_2O (25 μL, 1.4 mmol). The color of the solution turned orange-yellow. Volatile fractions were removed under reduced pressure, and the residual yellow solid was extracted into CH_2Cl_2 (6 mL). Insoluble fractions were filtered off, and Et_2O was allowed to diffuse into the filtrate to afford green-yellow blocks of **1** (320 mg, 48%). FTIR (KBr, cm^{-1}): 3649, 3632, 2966, 2906, 2870, 1602, 1562, 1513, 1487, 1446, 1409, 1385, 1364, 1294, 1215, 1170, 1069, 1041, 1019, 850, 808, 778, 753, 697, 636, 580, 514. UV−vis (CH_2Cl_2) (λ_{max}, nm (ϵ, M^{-1} cm^{-1})): 397 (2900). Anal. Calcd for $C_{76}H_{82}N_4O_{14}F_6Fe_4S_2$: C, 54.43; H, 4.93; N, 3.34; S, 3.82. Found: C, 54.47; H, 5.27; N, 3.17; S, 3.76.

$[Fe_4(\mu\text{-}OH)_4(\mu\text{-}O_2CAr^{4\text{-}tBuPh})_2(\mu\text{-}OTf)_2(4\text{-}^tBuC_5H_4N)_4]$ (2). This compound was prepared in a manner similar to that described for **1**, except that 4-*tert*-butylpyridine was used instead of pyridine. The reaction mixture was concentrated to an orange-yellow oil, which was extracted into CH_2Cl_2/PhCl (1:2) and filtered. Vapor diffusion of Et_2O into the filtrate afforded yellow crystals of **2** (42%). Yellow blocks suitable for X-ray crystallography were obtained by layering Et_2O over a saturated MeCN solution of this material. FTIR (KBr, cm^{-1}): 3645, 3634, 2966, 2906, 2870, 1615, 1566, 1513, 1502, 1458, 1421, 1384, 1367, 1294, 1273, 1220, 1170, 1071, 1020, 845, 830, 808, 781, 763, 734, 686, 637, 569, 516. UV−vis (CH_2Cl_2) (λ_{max}, nm (ϵ, M^{-1} cm^{-1})) 390 (3400). Anal. Calcd for $C_{76}H_{82}N_4O_{14}F_6Fe_4S_2$·$CH_2Cl_2$: C, 56.23; H, 5.89; N, 2.82. Found: C, 56.29; H, 6.33; N, 2.83.

$[Fe_4(\mu\text{-}OH)_4(\mu\text{-}O_2CAr^{4\text{-}tBuPh})_2(\mu\text{-}OTf)_2(3\text{-}FC_5H_4N)_4]$ (3). This compound was prepared in a manner similar to that described for **1**, except that 3-fluoropyridine was used instead of pyridine. Yellow blocks of **3** (70%) were obtained by vapor diffusion of pentane into a dichloromethane solution of this material and analyzed by X-ray crystallography. FTIR (KBr, cm^{-1}): 3644, 3630, 3064, 2966, 2907, 2870, 1608, 1587, 1555, 1514, 1481, 1457, 1435, 1410, 1385, 1365, 1295, 1255, 1236, 1216, 1173, 1120, 1099, 1017, 849, 836, 808, 778, 763, 695, 687, 636, 612, 580, 537, 515. UV−vis (CH_2Cl_2) (λ_{max}, nm (ϵ, M^{-1} cm^{-1})): 409 (3500). Anal. Calcd for $C_{76}H_{78}N_4O_{14}F_{10}Fe_4S_2$: C, 52.19; H, 4.50; N, 3.20. Found: C, 52.14; H, 4.87; N, 2.85.

X-ray Crystallographic Studies. Intensity data were collected on a Bruker (formerly Siemens) CCD diffractometer with graphite-monochromated Mo Kα radiation (λ = 0.71073 Å), controlled by a Pentium-based PC running the SMART software package.[31] Single crystals were mounted at room temperature on the tips of quartz fibers, coated with Paratone-N oil, and cooled to 188 K under a stream of cold nitrogen maintained by a Bruker LT-2A nitrogen cryostat. Data collection and reduction protocols are described elsewhere.[32] The structures were solved by direct methods and refined on F^2 by using the SHELXTL software package.[33] Empirical absorption corrections were applied with SADABS,[34] part of the SHELXTL program package. All non-hydrogen atoms were refined anisotropically unless otherwise noted. Hydrogen atoms were assigned idealized positions and given thermal parameters equivalent to either 1.5 (methyl hydrogen atoms) or 1.2 (all other hydrogen atoms) times the thermal parameter of the carbon atom to which they were attached. The hydrogen atoms associated with the bridging hydroxide ligands in **2** were located in the difference Fourier map and refined isotropically; those of the disordered solvent molecules were not included in the refinement. One of the butyl groups on the 4-*tert*-butylpyridine ligands in **2** was disordered over two positions. The atoms were equally distributed and refined isotropically. The lattice solvent molecules were modeled as partially occupied CH_2Cl_2 (0.25 occupancy) and Et_2O (0.75 occupancy) and refined isotropically. A half-occupied Et_2O was also found and

(26) Tolman, W. B.; Spencer, D. J. E. *Curr. Opin. Chem. Biol.* **2001**, *5*, 188−195.
(27) Pangborn, A. B.; Giardello, M. A.; Grubbs, R. H.; Rosen, R. K.; Timmers, F. J. *Organometallics* **1996**, *15*, 1518−1520.
(28) Hagen, K. S. *Inorg. Chem.* **2000**, *39*, 5867−5869.
(29) Du, C.-J. F.; Hart, H.; Ng, K.-K. D. *J. Org. Chem.* **1986**, *51*, 3162−3165.
(30) Saednya, A.; Hart, H. *Synthesis* **1996**, 1455−1458.
(31) *SMART v5.05*; Bruker AXS Inc.: Madison, WI, 1998.
(32) Feig, A. L.; Bautista, M. T.; Lippard, S. J. *Inorg. Chem.* **1996**, *35*, 6892−6898.
(33) Sheldrick, G. M. *SHELXTL v5.1: Program for the Refinement of Crystal Structures 97-2*; University of Göttingen: Göttingen, Germany, 1998.
(34) Sheldrick, G. M. *SADABS v2.03: Area-Detector Absorption Correction*; University of Göttingen: Göttingen, Germany, 1999.

Table 1. Summary of X-ray Crystallographic Data for $2\cdot0.25CH_2Cl_2\cdot1.25Et_2O$

empirical formula	$Fe_4C_{97.25}H_{114}N_4O_{15.25}Cl_{0.5}F_6S_2$
fw	2002.17
space group	$P2_1/c$
a, Å	20.9476(3)
b, Å	23.6601(4)
c, Å	20.9286(3)
α, deg	
β, deg	91.7110(10)
γ, deg	
V, Å^3	10368.1(3)
Z	4
ρ_{calcd}, g/cm^3	1.283
T, °C	−85
μ(Mo Kα), mm^{-1}	0.673
2θ limits, deg	3.9−50
total no. of data	76328
no. of unique data	18220
no. of params	1164
R1[a]	0.0598
wR2[b]	0.1434
max, min peaks, e/Å^3	1.149,[c] 0.518

[a] $R1 = \sum||F_o| - |F_c||/\sum|F_o|$. [b] $wR2 = \{\sum[w(F_o^2 - F_c^2)^2]/\sum[w(F_o^2)^2]\}^{1/2}$. [c] This peak occurs in the vicinity of a disordered dichloromethane molecule.

refined isotropically. Crystallographic information is provided in Table 1, and Figure S1 (Supporting Information) displays the structure of **2** with complete atom labeling schemes. The structures of **1** and **3** were not fully refined due to severe disorder in the bridging triflate anions and solvent molecules. Compound **1** crystallizes in orthorhombic space group $Pna2_1$ with $a = 20.1611(9)$ Å, $b = 19.6012(5)$ Å, $c = 22.1402(11)$ Å, $V = 8749.4(6)$ Å^3, and $Z = 4$. Compound **3** crystallizes in the same space group with $a = 20.191(2)$ Å, $b = 19.686(2)$ Å, $c = 22.071(3)$ Å, $V = 8773.0(18)$ Å^3, and $Z = 4$. Although detailed structural information is not provided, the core structures of **1** (Figure S2) and **3** (Figure S3) closely resemble that of **2**.

^{57}Fe Mössbauer Spectroscopy. Mössbauer spectra were obtained on an MS1 spectrometer (WEB Research Co.) with a ^{57}Co source in a Rh matrix maintained at room temperature in the MIT Department of Chemistry Instrumentation Facility. Solid samples were prepared by suspending ~0.02 mmol of the powdered material in Apeizon N grease and packing the mixture into a nylon sample holder. All data were collected at 4.2 K, and the isomer shift (δ) values are reported with respect to natural iron foil that was used for velocity calibration at room temperature. The spectra were fit to Lorentzian lines by using the WMOSS plot and fit program.[35]

Magnetic Susceptibility. The magnetic susceptibility of a polycrystalline powder of **1** was measured between 2 and 300 K with applied magnetic fields of 0.1 and 1 T using a Cryogenic S600 SQUID magnetometer. The sample was prepared under nitrogen, wrapped in Teflon, and quickly transferred to the SQUID vacuum chamber. Each measurement was repeated on two different samples to ensure reproducibility. The data were corrected for the magnetism of the sample holder, which was independently determined at the same temperature range and field. The underlying diamagnetism of the sample was estimated from Pascal's constants.[36] Magnetization measurements were performed on the same sample at 2.5 and 4.5 K with an applied field up to 6 T.

Electrochemistry. Cyclic voltammetric measurements were performed in a Vacuum Atmospheres drybox under nitrogen with an EG&G model 263 potentiostat. A three-electrode configuration consisting of a 1.75 mm^2 platinum working electrode, a $Ag/AgNO_3$ (0.1 M in MeCN with 0.5 M $(Bu_4N)(PF_6)$) reference electrode, and a platinum mesh auxiliary electrode was used. The supporting electrolyte was 0.5 M $(Bu_4N)(PF_6)$ in CH_2Cl_2. All cyclic voltammograms were externally referenced to the Cp_2Fe/Cp_2Fe^+ couple.

(35) Kent, T. A. *WMOSS: Mössbauer Spectral Analysis Software*, v 2.5; WEB Research Co.: Minneapolis, 1998.
(36) Carlin, R. L. *Magnetochemistry*; Springer-Verlag: New York, 1986.

Scheme 1

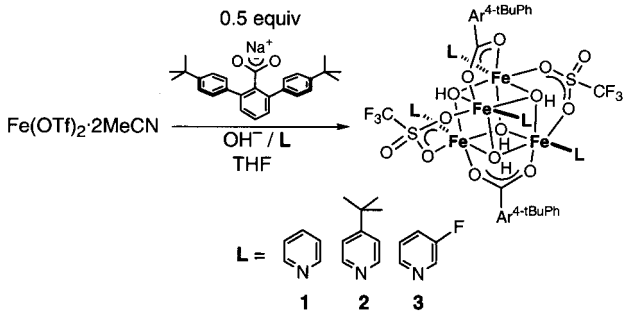

Results

Synthesis and Structural Characterization of $[Fe_4(\mu\text{-}OH)_4(\mu\text{-}O_2CAr^{4\text{-}tBuPh})_2(\mu\text{-}OTf)_2L_4]$ (L = C_5H_5N (1), 4-^{t}BuC_5H_4N (2), and 3-FC_5H_4N (3)). Reaction of $Fe(OTf)_2\cdot2MeCN$, $NaO_2CAr^{4\text{-}tBuPh}$, OH^-, and pyridine derivatives in a 2:1:2:2 ratio in THF afforded neutral tetrairon(II) clusters (Scheme 1). Extremely air-sensitive yellow blocks of **1**−**3** were obtained in modest to good yield (42−70%) following recrystallization from CH_2Cl_2/Et_2O. Although the solid-state structures of **1**−**3** were unambiguously determined by X-ray crystallography (Figures 1 and S1−S3), severe disorder in the bridging triflate ligands and solvent molecules hampered detailed structural refinement of the models for **1** and **3**.

The crystal structure of **2** is shown in Figure 1; selected bond lengths and angles are listed in Table 2. Compound **2** has a $\{Fe_4(\mu\text{-}OH)_4\}^{4+}$ core, which can be best described as interpenetrating Fe_4 and $(OH)_4$ disphenoids. Each iron atom occupies alternating vertexes of the resulting cube and has distorted octahedral geometry with a NO_5 donor atom set (Table 2). The assignment of the single-atom bridging ligand as hydroxide is supported by the Fe−O distances, which range from 2.081(3) to 2.154(3) Å, as well as by the location and refinement of the associated hydrogen atoms in the X-ray structure determination. Comparable $Fe-O_{hydroxo}$ distances occur in other high-spin iron(II) complexes.[37−39]

The $\{Fe_4(\mu\text{-}OH)_4(\mu\text{-}O_2CAr^{4\text{-}tBuPh})_2(\mu\text{-}OTf)_2\}$ core in **2** can be visualized as arising from the formal dimerization of two orthogonal $\{Fe_2(\mu\text{-}OH)_2(\mu\text{-}O_2CAr^{4\text{-}tBuPh})\}^+$ units, assisted by two μ-1,3 triflate ligands. The arrangement of ancillary ligands encapsulating the cubic core is such that the local point group symmetry of **2** is reduced from T_d to D_2. As a result, **2** can occur in two enantiomeric forms, which crystallize as a racemic mixture. The two μ-1,3 carboxylate ligands span each diiron(II) unit on parallel faces of a cube, minimizing steric interactions between the bulky 4-*tert*-butylphenyl groups. Such steric interactions apparently play a crucial role in assembling the $\{Fe_4(OH)_4\}^{4+}$ cores. When attempts were made to access this unit with the sterically less demanding carboxylate ligand 2,6-di(*p*-tolyl)benzoate ($Ar^{Tol}CO_2^-$), only a paddlewheel diiron(II) complex, $[Fe_2(\mu\text{-}O_2CAr^{Tol})_4(4\text{-}^tBuC_5H_4N)_2]$,[17] was isolated under similar reaction conditions.

Depending on the nature of the bridging ligands, systematic variations in the Fe···Fe separations are observed. As shown in Figure 1, three different types of diiron(II) subunits are

(37) Hartman, J. R.; Rardin, R. L.; Chaudhuri, P.; Pohl, K.; Wieghardt, K.; Nuber, B.; Weiss, J.; Papaefthymiou, G. C.; Frankel, R. B.; Lippard, S. J. *J. Am. Chem. Soc.* **1987**, *109*, 7387−7396.
(38) Kitajima, N.; Tamura, N.; Tanaka, M.; Moro-oka, Y. *Inorg. Chem.* **1992**, *31*, 3342−3343.
(39) MacMurdo, V. L.; Zheng, H.; Que, L., Jr. *Inorg. Chem.* **2000**, *39*, 2254−2255.

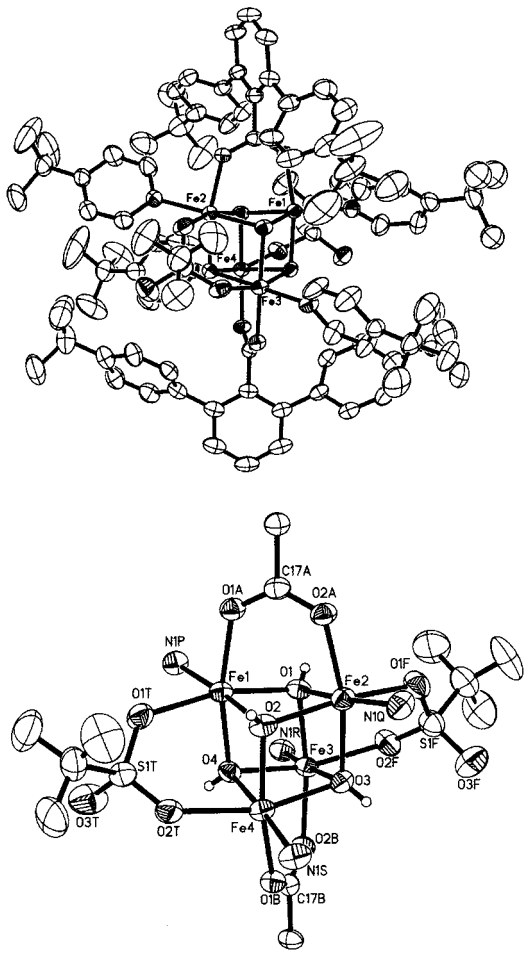

Figure 1. ORTEP diagram of $[Fe_4(\mu\text{-}OH)_4(\mu\text{-}O_2CAr^{4\text{-}tBuPh})_2(\mu\text{-}OTf)_2(4\text{-}^tBuC_5H_4N)_4]$ (**2**) with thermal ellipsoids at 50% probability: top, whole molecule; bottom, core structure.

identified in **2**. They are $\{Fe_2(\mu\text{-}OH)_2\}^{2+}$, $\{Fe_2(\mu\text{-}OH)_2(\mu\text{-}OTf)\}^{+}$, and $\{Fe_2(\mu\text{-}OH)_2(\mu\text{-}O_2CAr^{4\text{-}tBuPh})\}^{+}$. The Fe···Fe distances decrease with increasing numbers of bridging ligands (Table 2). Compared with the intermetallic distances in the $\{Fe_2(\mu\text{-}OH)_2\}^{2+}$ pairs (Fe1···Fe3, Fe2···Fe4), those in the $\{Fe_2(\mu\text{-}OH)_2(\mu\text{-}OTf)\}^{+}$ units (Fe1···Fe4, Fe2···Fe3) are reduced by ca. 0.08 Å. These separations are further shortened by ca. 0.10 Å when the bridging triflate is replaced by a carboxylate (Fe1···Fe2, Fe3···Fe4). The differences in the O−X (X = C or S) distances, rather than the Fe−O−X (X = C or S) angles, of the bridging ligands are responsible for such a core contraction. The O−C distances (1.255(5)−1.268(5) Å) are significantly shorter than the O−S distances (1.452(3)−1.457(3) Å), whereas the Fe−O−C angles (126.3(2)−129.7(2)°) are comparable to the Fe−O−S angles (122.60(17)−127.10(17)°). As expected, a decrease in the Fe···Fe distances is accompanied by a diminution in the Fe−O−Fe angles in the $\{Fe_2(\mu\text{-}OH)_2\}^{2+}$ rhombuses (Table 2), which may affect the overlap between orbitals participating in magnetic exchange interactions (vide infra).

Electronic Absorption Spectroscopy. Compounds **1**−**3** exhibit intense visible absorption bands at λ_{max} = 390−409 nm (Figure 2), which are assigned as MLCT transitions[40] by analogy to the similar transitions at ∼360 nm in related Fe(II)−pyridine units.[41] The observed red shift in the electronic spectra with increasingly more electron-withdrawing pyridine derivatives, 4-*tert*-butylpyridine < pyridine < 3-fluoropyridine, is consistent with such an assignment. The magnitude of ϵ per Fe−pyridine unit (725−875 M^{-1} cm^{-1}) is comparable to that of other iron(II) complexes having similar ligand combinations.[41]

Table 2. Selected Bond Lengths (Å) and Angles (deg) for **2**[a]

bond length		bond angle	
Fe(1)···Fe(2)	3.0714(8)	Fe(1)−O(1)−Fe(2)	92.61(12)
Fe(1)···Fe(3)	3.2447(8)	O(1)−Fe(2)−O(2)	85.35(12)
Fe(1)···Fe(4)	3.1700(8)	Fe(1)−O(2)−Fe(2)	92.21(11)
Fe(2)···Fe(3)	3.1647(8)	O(1)−Fe(1)−O(2)	85.66(12)
Fe(2)···Fe(4)	3.2508(8)	Fe(1)−O(1)−Fe(3)	101.53(14)
Fe(3)···Fe(4)	3.0605(8)	O(1)−Fe(3)−O(4)	78.84(12)
Fe(1)−O(1)	2.108(3)	Fe(1)−O(4)−Fe(3)	100.40(13)
Fe(1)−O(2)	2.141(3)	O(1)−Fe(1)−O(4)	79.23(12)
Fe(1)−O(4)	2.090(3)	Fe(1)−O(2)−Fe(4)	97.26(12)
Fe(1)−O(1A)	2.100(3)	O(2)−Fe(4)−O(4)	82.54(11)
Fe(1)−O(1T)	2.231(3)	Fe(1)−O(4)−Fe(4)	97.41(12)
Fe(1)−N(1P)	2.157(3)	O(4)−Fe(1)−O(2)	82.06(11)
Fe(2)−O(1)	2.140(3)	Fe(2)−O(1)−Fe(3)	97.11(13)
Fe(2)−O(2)	2.121(3)	O(1)−Fe(3)−O(3)	82.36(12)
Fe(2)−O(3)	2.076(3)	Fe(2)−O(3)−Fe(3)	97.68(12)
Fe(2)−O(2A)	2.084(3)	O(3)−Fe(2)−O(1)	82.17(12)
Fe(2)−O(1F)	2.263(3)	Fe(4)−O(2)−Fe(2)	101.31(13)
Fe(2)−N(1Q)	2.154(3)	O(2)−Fe(4)−O(3)	78.69(11)
Fe(3)−O(1)	2.081(3)	Fe(2)−O(3)−Fe(4)	100.42(13)
Fe(3)−O(3)	2.127(3)	O(2)−Fe(2)−O(3)	79.59(11)
Fe(3)−O(4)	2.133(3)	Fe(3)−O(3)−Fe(4)	91.26(11)
Fe(3)−O(2B)	2.080(3)	O(4)−Fe(4)−O(3)	86.16(11)
Fe(3)−O(2F)	2.260(3)	Fe(4)−O(4)−Fe(3)	91.80(12)
Fe(3)−N(1R)	2.151(3)	O(3)−Fe(3)−O(4)	86.73(11)
Fe(4)−O(2)	2.082(3)		
Fe(4)−O(3)	2.154(3)		
Fe(4)−O(4)	2.129(3)		
Fe(4)−O(1B)	2.078(3)		
Fe(4)−O(2T)	2.281(3)		
Fe(4)−N(1S)	2.159(3)		

[a] Number in parentheses are estimated standard deviations of the last significant figure. Atoms are labeled as indicated in Figure 1.

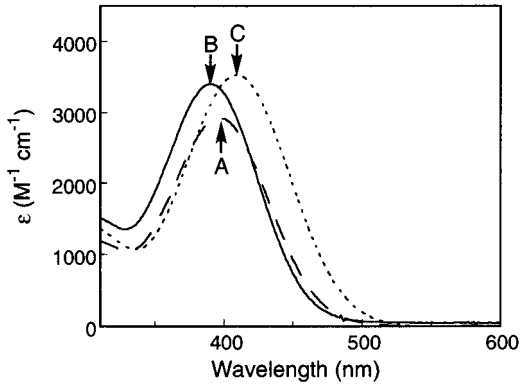

Figure 2. Electronic absorption spectra of **1**−**3** showing the MLCT transitions: (A) $[Fe_4(\mu\text{-}OH)_4(\mu\text{-}O_2CAr^{4\text{-}tBuPh})_2(\mu\text{-}OTf)_2(C_5H_5N)_4]$ (**1**) (—); (B) $[Fe_4(\mu\text{-}OH)_4(\mu\text{-}O_2CAr^{4\text{-}tBuPh})_2(\mu\text{-}OTf)_2(4\text{-}^tBuC_5H_4N)_4]$ (**2**) (---); (C) $[Fe_4(\mu\text{-}OH)_4(\mu\text{-}O_2CAr^{4\text{-}tBuPh})_2(\mu\text{-}OTf)_2(3\text{-}FC_5H_4N)_4]$ (**3**) (···).

IR Spectroscopy. IR spectra of **1**−**3** display strong absorptions at 3630−3649 cm^{-1}, attributable to the stretching vibrations of the coordinated hydroxide ligands.[42] As shown in Figure 3A, two sharp ν_{OH} bands occur at 3632 and 3649 cm^{-1} for a solid sample of **1**. The corresponding ν_{OD} frequencies appear at 2681 and 2691 cm^{-1} for a sample prepared with deuterium-

(40) Lever, A. B. P. *Inorganic Electronic Spectroscopy*, 2nd ed.; Elsevier Science Publishers B.V.: Amsterdam, The Netherlands, 1984.

(41) LeCloux, D. D.; Barrios, A. M.; Mizoguchi, T. J.; Lippard, S. J. *J. Am. Chem. Soc.* **1998**, *120*, 9001−9014.

(42) Nakamoto, K. *Infrared and Raman Spectra of Inorganic and Coordination Compounds*, 5th ed.; Wiley-Interscience: New York, 1997.

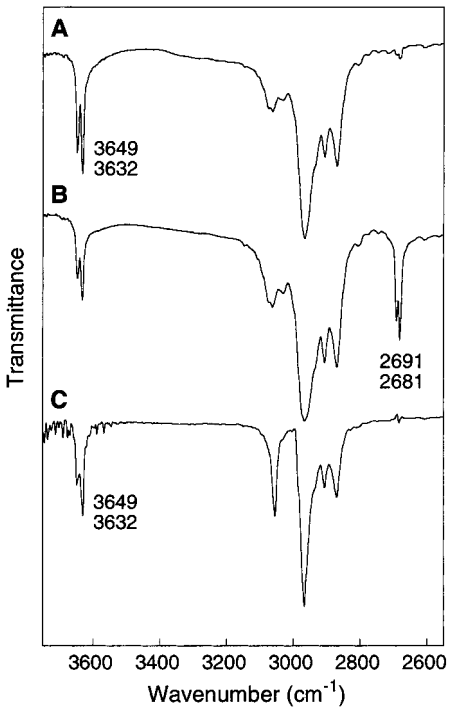

Figure 3. IR spectra of $[Fe_4(\mu\text{-}OH)_4(\mu\text{-}O_2CAr^{4\text{-}tBuPh})_2(\mu\text{-}OTf)_2(C_5H_5N)_4]$ **1**; (A) in KBr; (B) in KBr as a mixture with a OD^--substituted cluster, $[Fe_4(\mu\text{-}OD)_4(\mu\text{-}O_2CAr^{4\text{-}tBuPh})_2(\mu\text{-}OTf)_2(C_5H_5N)_4]$; (C) in CH_2Cl_2.

enriched water (Figure 3B), which presumably afforded a mixture comprising $[Fe_4(\mu\text{-}OD)_n(\mu\text{-}OH)_{4-n}(\mu\text{-}O_2CAr^{4\text{-}tBuPh})_2(\mu\text{-}OTf)_2(C_5H_5N)_4]$ ($n = 0-4$). The observed shifts in hydroxide stretching frequencies upon OH to OD substitution ($\Delta\nu_{obsd}$ = 951 and 958 cm^{-1}) are close to those expected from a simple diatomic oscillator model ($\Delta\nu_{calc}$ = 989 and 994 cm^{-1}). Lowering the local symmetry of $\{Fe_4(\mu\text{-}OH)_4\}^{4+}$ from T_d to D_2 would result in the splitting of a single IR-active OH stretching mode (T_2) into three active components (B_1, B_2, and B_3), two of which are apparently degenerate. The integrity of the $\{Fe_4(\mu\text{-}OH)_4\}^{4+}$ core in solution was probed by IR spectroscopy in CH_2Cl_2. As shown in Figure 3C, the characteristic OH vibrations of **1** at 3632 and 3649 cm^{-1} are retained with the same relative intensities as those in the solid sample. This result indicates that the cubane structure remains intact in solution and that the splitting of the OH stretches observed in the solid state does not originate from intermolecular interactions or other solid-state effects.

^{19}F NMR Spectroscopy. The presence of fluorine nuclei in the bridging triflate and 3-fluoropyridine ligands allowed the use of ^{19}F NMR spectroscopy to investigate further the solution structures of **1** and **3**. ^{19}F NMR spectroscopy is a good structural probe for paramagnetic iron(II) or cobalt(II) clusters, from which the number and symmetry of the species in solution can often be inferred.[43-46] In CH_2Cl_2 at 20 °C, **1** exhibits a single broad ($\Delta\nu_{1/2}$ = 393 Hz) resonance at 55.0 ppm (Figure 4A). This signal arises from the μ-1,3 triflate ligands, which are related by pseudo-C_2 symmetry, and is significantly downfield shifted from that (−79.2 ppm) of the free anion, measured independently as a tetrabutylammonium salt. A similar paramagnetic shift to 60.4 ppm was reported for a triflate anion bridging two high-spin iron(II) centers, which is significantly downfield from that of a terminal monodentate triflate (−14.0 ppm).[46] This behavior appears to reflect the proximity of the fluorine nuclei to two paramagnetic centers.

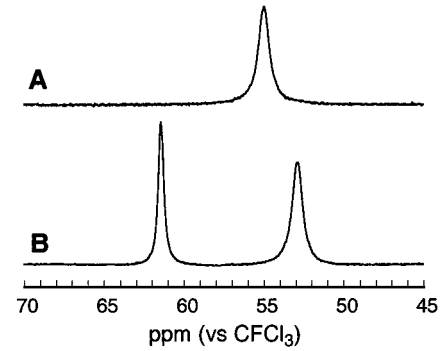

Figure 4. ^{19}F NMR (470 MHz) spectra (vs $CFCl_3$ at 20 °C) of $[Fe_4(\mu\text{-}OH)_4(\mu\text{-}O_2CAr^{4\text{-}tBuPh})_2(\mu\text{-}OTf)_2(C_5H_5N)_4]$ (**1**) (A) and $[Fe_4(\mu\text{-}OH)_4(\mu\text{-}O_2CAr^{4\text{-}tBuPh})_2(\mu\text{-}OTf)_2(3\text{-}FC_5H_4N)_4]$ (**3**) (B) in CH_2Cl_2.

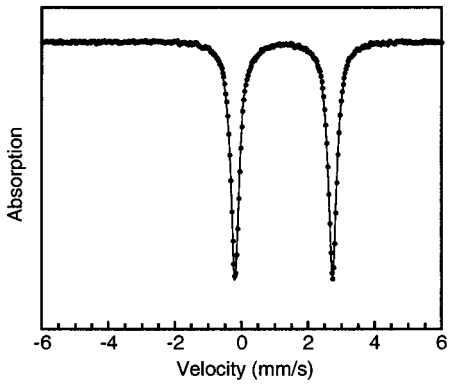

Figure 5. Zero-field Mössbauer spectrum (experimental data (•), calculated fit (−)) recorded at 4.2 K for $[Fe_4(\mu\text{-}OH)_4(\mu\text{-}O_2CAr^{4\text{-}tBuPh})_2(\mu\text{-}OTf)_2(C_5H_5N)_4]$ (**1**) in the solid state.

Under similar conditions, **3** displays two resonances at 52.9 and 61.4 ppm (Figure 4B) that arise from the triflate and the 3-fluoropyridine ligands, respectively. Such an assignment is supported by the breadth ($\Delta\nu_{1/2}$ = 366 Hz) of the 52.9 ppm resonance, which is comparable to that of the OTf^- signal in **1**, as well as by a ∼3:2 ratio of the integrated intensities. No signal was detected for unbound triflate (−79.2 ppm) or 3-fluoropyridine (−127.6 ppm). The presence of lower or higher nuclearity species in the solution is unlikely based on the simplicity of the ^{19}F NMR pattern, which is consistent with the solid-state structure of **3**.

Mössbauer Spectroscopy. Figures 5 and S4 display zero-field Mössbauer spectra of the solid samples of **1**−**3** measured at 4.2 K; the corresponding parameters derived from fits of the spectra are provided in Table 3 along with those of topologically related tetrairon(II) complexes. Although there are four crystallographically unique iron sites in **1**−**3**, their nearly identical coordination environments produce unresolved Mössbauer spectra. No attempts were made to deconvolute further the single sharp ($\Gamma \approx 0.30$ mm s^{-1}) quadrupole doublets. The isomer shifts and quadrupole splittings of **1**−**3** are typical of high-spin iron(II) sites in a N/O coordination environment[10,47,48] and comparable

(43) Hagen, K. S.; Lachicotte, R.; Kitaygorodskiy, A.; Elbouadili, A. *Angew. Chem., Int. Ed. Engl.* **1993**, *32*, 1321−1324.
(44) Lachicotte, R.; Kitaygorodskiy, A.; Hagen, K. S. *J. Am. Chem. Soc.* **1993**, *115*, 8883−8884.
(45) Hagen, K. S.; Lachicotte, R.; Kitaygorodskiy, A. *J. Am. Chem. Soc.* **1993**, *115*, 12617−12618.
(46) Blakesley, D. W.; Payne, S. C.; Hagen, K. S. *Inorg. Chem.* **2000**, *39*, 1979−1989.
(47) Gütlich, P.; Ensling, J. In *Inorganic Electronic Structure and Spectroscopy*; Solomon, E. I., Lever, A. B. P., Eds.; John Wiley & Sons: New York, 1999; Vol. I, pp 161−211.

Table 3. Zero-Field Mössbauer Parameters for **1**−**3** and Related Tetrairon(II) Clusters

compound	T (K)	δ (mm s^{-1})	ΔE_Q (mm s^{-1})	Γ (mm s^{-1})	ref
1	4.2	1.27(2)	2.93(2)	0.30	this work
2	4.2	1.26(2)	3.00(2)	0.30	this work
3	4.2	1.27(2)	2.96(2)	0.31	this work
[Fe(OMe)(MeOH)(DPM)]$_4$	4.2	1.25	2.35	0.44	14
[Fe(OMe)(MeOH)(DBM)]$_4$	80	1.21	2.52	0.30	14

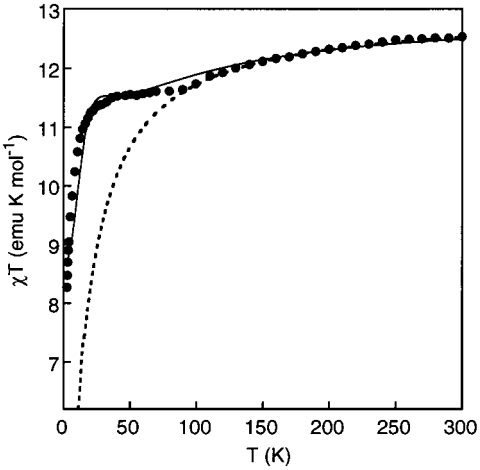

Figure 6. χT versus temperature for [Fe$_4$(μ-OH)$_4$(μ-O$_2$CAr$^{4\text{-}t\text{Buph}}$)$_2$(μ-OTf)$_2$(C$_5$H$_5$N)$_4$] (**1**) (●). The dashed line is the calculated χT values with the two different isotropic Hamiltonians as described in the text (models A and B; see the text), which afforded two superimposable curves. The solid line was obtained by using the following parameters: $J = 1.2$ cm^{-1}; $D = -7.0$ cm^{-1} ($S = 4$); $D = 5.7$ cm^{-1} ($S = 5$); $D = 3.5$ cm^{-1} ($S = 6$); $D = -2.1$ cm^{-1} ($S = 8$). See the text for the details of the calculation.

to those obtained for related {Fe$_4$(OR)$_4$}$^{4+}$ cores (Table 3). The similar Mössbauer parameters obtained for **1**−**3** suggest that the electronic environment around the metal center is not significantly perturbed upon changing the nitrogen donor ligands. This result is also consistent with the minimal structural variations observed in the solid-state structures of **1**−**3**.

Magnetochemistry. The χT vs T curve for **1** is depicted in Figure 6; the magnetization curves at 2.5 and 4.5 K are displayed in Figure S5. The measured value of $\chi T = 12.6$ emu K mol^{-1} at 300 K is consistent with the presence of four uncoupled $S = 2$ centers with $g = 2.08$ (expected value of $\chi T = 12.9$ emu K mol^{-1}), which is slightly lower than those usually observed for high-spin iron(II) ions.[36,49,50] Upon lowering the temperature, χT gradually decreases and reaches a plateau of 11.64 emu K mol^{-1} between 90 and 35 K. From 35 to 2 K, however, the value drops from 11.50 to 8.3 emu K mol^{-1}. This relatively high χT value indicates that excited magnetic states are still populated at the lowest temperature. This observed magnetic behavior is not easy to rationalize because of the orbitally degenerate ground state ($^5T_{2g}$) of high-spin octahedral iron(II), which complicates the interpretation of the magnetic data. With a deviation from ideal octahedral geometry, however, the orbital contribution is significantly quenched[51] and its effect on the temperature dependence of the magnetic moment is expected to be very small.[36,49] Another complicating feature of iron(II) complexes is their large zero-field splitting (ZFS) effects (up to ~20 cm^{-1}),[52] which can affect the χT behavior even at quite high temperatures. In the case of exchange-coupled systems, the ZFS and exchange coupling are often of the same order of magnitude, which makes the interpretation of the magnetic data even less straightforward. Given all these features, only a semiquantitative explanation for the magnetic behavior of **1** was possible.

To minimize the effects from ZFS, only the high-temperature region (>90 K) of the curve was analyzed as a first approximation. A similar approach has been used for a related class of compounds, which exhibit a weak ferromagnetic coupling.[14] In this framework, it is obvious that the decrease in χT observed in this region can be attributed to weak antiferromagnetic (AF) coupling between the four magnetic centers. As a first step, we assumed T_d symmetry for the coupling and neglected the differences in the Fe−O−Fe angles and Fe···Fe distances in the cubane structure (model A). By applying the Hamiltonian

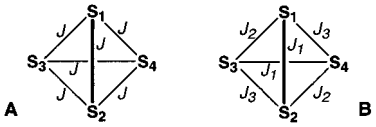

in eq 1, the best fit was obtained for $J = 1.2$ cm^{-1} and $g = 2.08$ (Figure 6). This treatment affords a $S = 0$ ground state, with the difference in energy between two states being $\Delta E = JS(S + 1)/2$.

$$\mathscr{H} = J(\mathbf{S}_1\cdot\mathbf{S}_2 + \mathbf{S}_1\cdot\mathbf{S}_3 + \mathbf{S}_1\cdot\mathbf{S}_4 + \mathbf{S}_2\cdot\mathbf{S}_3 + \mathbf{S}_2\cdot\mathbf{S}_4 + \mathbf{S}_3\cdot\mathbf{S}_4) \quad (1)$$

Alternatively, the six Fe···Fe exchange paths can be grouped into three pairs, each of them experiencing different exchange coupling (model B). This subdivision can be made on the basis of either the bridging topology and the corresponding Fe···Fe distances or the values of the Fe−O−Fe angles. For either choice, the Hamiltonian in eq 2 describes the coupling interac-

$$\mathscr{H} = J_1(\mathbf{S}_1\cdot\mathbf{S}_2 + \mathbf{S}_3\cdot\mathbf{S}_4) + J_2(\mathbf{S}_1\cdot\mathbf{S}_3 + \mathbf{S}_2\cdot\mathbf{S}_4) + J_3(\mathbf{S}_1\cdot\mathbf{S}_4 + \mathbf{S}_2\cdot\mathbf{S}_3) \quad (2)$$

tions. This approach yielded for the best fit (Figure 6) the coupling constants $J_1 = 1.74$ cm^{-1}, $J_2 = 1.33$ cm^{-1}, and $J_3 = 0.35$ cm^{-1}, with $g = 2.08$. Assuming that the $\mathbf{S}_1-\mathbf{S}_2/\mathbf{S}_3-\mathbf{S}_4$ pairs are the triply bridged {Fe$_2$(μ-OH)$_2$(μ-O$_2$CAr$^{4\text{-}t\text{Buph}}$)}$^+$ units, $\mathbf{S}_1-\mathbf{S}_3/\mathbf{S}_2-\mathbf{S}_4$ are the triply bridged {Fe$_2$(μ-OH)$_2$(μ-OTf)}$^+$ units, and $\mathbf{S}_1-\mathbf{S}_4/\mathbf{S}_2-\mathbf{S}_3$ are the doubly bridged {Fe$_2$(μ-OH)$_2$}$^{2+}$ units, the trend is consistent with increasing AF interaction with decreasing Fe···Fe distances (and decreasing Fe−O−Fe angles). As mentioned above, however, the differences in the coupling constants can also originate from the differences in the Fe−O−Fe angles. In particular, the AF interactions should increase with increasing angles, which would strengthen the overlap

(48) Münck, E. In *Physical Methods in Bioinorganic Chemistry: Spectroscopy and Magnetism*; Que, L., Jr., Ed.; University Science Books: Sausalito, CA, 2000; pp 287−319.
(49) *Theory and Applications of Molecular Paramagnetism*; Boudreaux, E. A., Mulay, L. N., Eds.; Wiley-Interscience: New York, 1976.
(50) Girerd, J.-J.; Journaux, Y. In *Physical Methods in Bioinorganic Chemistry: Spectroscopy and Magnetism*; Que, L., Jr., Ed.; University Science Books: Sausalito, CA, 2000; pp 321−374.
(51) Borrás-Almenar, J. J.; Clemente-Juan, J. M.; Coronado, E.; Palii, A. V.; Tsukerblat, B. S. *J. Phys. Chem. A* **1998**, *102*, 200−213.
(52) Varret, F. *J. Phys. Chem. Solids* **1976**, *37*, 257−263.

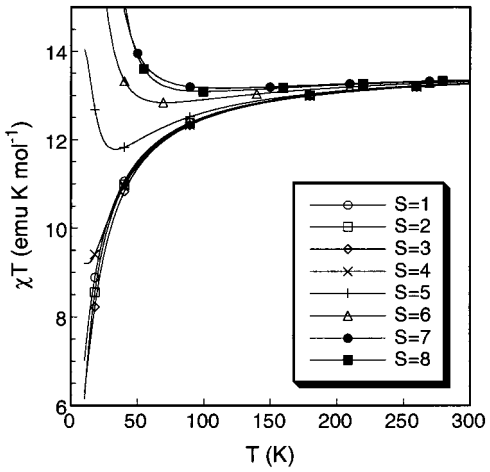

Figure 7. Calculated χT versus T for $S = 1-8$ with $D = 5$ cm^{-1}. Whereas ZFS has only a small effect for lower multiplicity states ($S = 1-3$), its contribution becomes significant for the higher multiplicity states ($S = 4-8$).

between the orbitals of the metals involved in magnetic coupling. The AF interactions decrease with increasing Fe···Fe distance, however. Thus, the differences between the coupling constants, $|J_1 - J_2| = 0.41$ cm^{-1} and $|J_2 - J_3| = 0.98$ cm^{-1}, favor the former interpretation. The two larger coupling constants (J_1 and J_2) are of similar magnitude and may be affected by coupling pathways mediated by the $Ar^{4\text{-}tBuPh}CO_2^-$ and OTf^- bridging ligands. Such pathways are not available for J_3. As described below, however, care should be exercised not to overinterpret these results for the general purpose of evolving a magneto-structural correlation,[14] given the large number of parameters used to describe the magnetic behavior of this system.

The coupling interactions modeled above are unable to reproduce the experimental data at lower temperatures. The simulated χT curve significantly deviates from the experimental data below 90 K. To obtain a reasonable simulation for this region, ZFS effects were introduced. For the sake of simplicity, we assumed an energy level pattern based on the one-J model (model A). Even with this approach the number of parameters is still quite large because there are eight levels ($S = 1-8$) that are affected by ZFS. Accordingly, only a qualitative analysis of these effects on the calculated curves could be performed. As shown in Figure 7, a value of $D = 5$ cm^{-1}, chosen arbitrarily because it lies in the expected range for an iron(II) center, for the higher spin states can significantly affect the calculated χT curve, which deviates from the "isotropic" one even at 100 K. Since ZFS apparently increases the magnetic moment at lower temperatures, the experimentally observed behavior may be explained by invoking a subtle balance between exchange coupling and anisotropy, a quantitative determination of which poses a significant challenge. A more detailed analysis should also consider the difference between the three coupling pathways and introduce an anisotropic **g** tensor,[53] which would eventually result in overparametrization of the system and a large correlation between the obtained values, possibly leading to meaningless results.

We therefore conclude that the observed magnetic behavior of **1** results from weak AF coupling between the iron(II) centers, which is accompanied by large ZFS of the excited states. A theoretical curve can be constructed from this model that reproduces the plateau between 90 and 35 K observed experimentally (Figure 6). In support of this model, the magnetization curves (Figure S5) clearly indicate that the complex is far from saturation even at 6 T and low temperature (2.5 K). Such behavior further supports the conclusion that weak AF coupling occurs between magnetic centers and that significant ZFS arises from different excited states that are populated at low temperatures.

(53) Belanzoni, P.; Re, N.; Rosi, M.; Sgamellotti, A.; Baerends, E. J.; Floriani, C. *Inorg. Chem.* **1996**, *35*, 7776−7785.

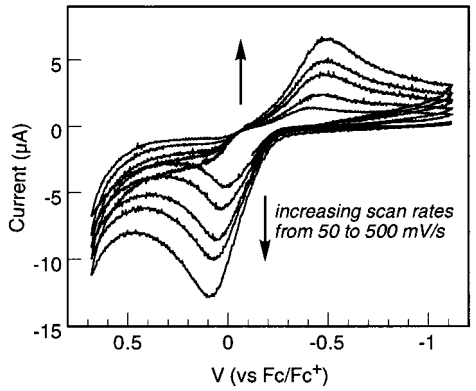

Figure 8. Cyclic voltammograms of $[Fe_4(\mu\text{-}OH)_4(\mu\text{-}O_2CAr^{4\text{-}tBuPh})_2(\mu\text{-}OTf)_2(C_5H_5N)_4]$ (**1**) in CH_2Cl_2 with 0.5 M $(Bu_4N)(PF_6)$ as supporting electrolyte. Scan rates vary from 50 to 500 mV/s.

Electrochemistry. Cyclic voltammograms of a CH_2Cl_2 solution of **1** reveal an oxidation at −10 mV vs Cp_2Fe/Cp_2Fe^+. A broad second oxidation wave occurs at 880 mV, which does not display a corresponding reduction wave in the return sweep (Figure S6). The presence of two separate cathodic peaks at −420 and −810 mV prompted us to investigate whether these reduction processes may be related to the first oxidation step. With a potential sweep range from −1100 to +700 mV, the first oxidation step approaches quasi-reversible behavior with increased scan rates (Figure 8). At a scan rate of 500 mV/s, the oxidation and reduction peaks maximize at +90 and −490 mV, respectively.

Discussion

Three complexes stabilizing the novel $\{Fe_4(\mu\text{-}OH)_4\}^{4+}$ core were readily synthesized with the use of sterically encumbering terphenyl carboxylate ligands. These complexes are stable both in the solid state and in solution when protected from exposure to dioxygen or other oxidizing agents.

Four metal ions and four bridging ligands positioned at alternating corners of a cube describe a well-known unit in inorganic chemistry.[14] Compared with other transition metal ions, however, access to cubic compounds containing oxygen-derived single-atom bridging ligands has been quite limited in iron chemistry. There are only four examples of tetrairon(II) clusters having $\{Fe_4(\mu\text{-}OR)_4\}^{n+}$ core fragments. They are $[Fe_4(DBCat)_4(py)_6]$,[13] $[Fe(OMe)(MeOH)(DBM)]_4$,[14] $[Fe(OMe)(MeOH)(DPM)]_4$,[14] and $[Fe_4(sae)_4(MeOH)_4]$,[15] where $DBCatH_2$ = 3,5-di-*tert*-butylcatechol, HDBM = dibenzoylmethane, HDPM = dipivaloylmethane, and H_2sae = 2-salicylideneamino-1-ethanol. The single-atom bridging ligands in each of these compounds are derived from either alkoxide or phenoxide ions. Compounds **1**−**3** represent the first examples of a tetrairon cube having bridging hydroxo ligands, which significantly expands the class of cubic polyiron clusters. Analogous compounds with $\{M_4(\mu\text{-}OH)_4\}^{n+}$ units occur for most first low transition metals including chromium,[54] manganese,[55] cobalt,[56] nickel,[57] and copper.[58]

Interpretation of the magnetic behavior of compound **1** was complicated by significant anisotropy, ZFS, and orbital contri-

butions related with the $^5T_{2g}$ ground state of iron(II). Although a unique set of magnetic parameters cannot be provided, weak AF coupling and substantial ZFS are evident. Related tetrairon(II) clusters with alkoxide bridging groups, $[Fe(OMe)(MeOH)(DPM)]_4$[14] and $[Fe_4(sae)_4(MeOH)_4]$,[15] display weak ferromagnetic interactions among the iron(II) centers, affording a $S = 8$ ground state. The different number of exchange pathways render magnetostructural correlations less than straightforward, but it would appear that triply bridging methoxide or hydroxide ligands do not provide an efficient exchange coupling pathway between the linked iron(II) centers. Subtle geometrical differences in the M−O−M and O−M−O angles as well as the M···M distances may trigger crossover from ferromagnetic to antiferromagnetic interactions within the $\{Fe_4(OR)_4\}^{4+}$ module.

The quasi-reversible electrochemical behavior of **1** at high scan rates, along with the $(E_a - E_c)$ dependence on scan rate, indicates that structural rearrangements may accompany oxidation of the tetrairon(II) core. The increased acidity of the oxidized metal centers will favor deprotonation of the bridging hydroxo groups, a phenomenon well documented for (μ-hydroxo)diiron(II) complexes.[37,59] Structural instability of the $\{Fe_4(\mu\text{-}OH)_4\}^{4+}$ core upon a change in oxidation state would be a significant liability if such units were to be used for biological ET reactions. To lower the Franck−Condon barrier for ET, minimal inner-sphere reorganization is desirable.[60] Both synthetic modeling[1,61,62] and theoretical calculations[63] point toward minimal structural changes in $\{Fe_4(\mu\text{-}S)_4\}^{n+}$ centers at different physiological oxidation states.

In this context, it is worth noting the electrochemical behavior of a $\{Fe_4(\mu\text{-}O)_4\}^{4+}$ unit embedded in an octairon(III) cluster $[Fe_8(\mu\text{-}O)_4(\mu\text{-}pz)_{12}Cl_4]$; here, an oxo-bridged tetrairon(III) cuboidal fragment is buried inside an "Fe−pyrazolate (pz) coat".[12] In CH_2Cl_2 solution this compound can be sequentially reduced in one-electron steps from tetrairon(III) to tetrairon(II). The first three reduction processes are electrochemically reversible, indicating that no geometric rearrangement accompanies ET. This unusual stability was ascribed to the encapsulation of the $\{Fe_4(\mu\text{-}O)_4\}^{n+}$ core within an inert shell that forces its structural integrity. It should be noted, however, that the bridging oxo groups in this cluster are coordinated to iron(III) sites comprising the "inert shell", which may help dissipate the developing charge following electrochemical reduction of the core unit. In the absence of such confinement, it is not clear whether the $\{Fe_4(\mu\text{-}O)_4\}^{n+}$ core can undergo similarly reversible redox processes. Discrete tetrairon cubane-type clusters having oxo bridging ligands are yet to be prepared.

With the recent spectroscopic identification[64] as well as crystallographic characterization[65] of the all-ferrous iron cube in the Fe protein of the nitrogenase system, the functionally relevant oxidation states of the biological [4Fe−4S] clusters now span from Fe^{II}_4 to $Fe^{II}Fe^{III}_3$. Although such oxidation states can be accessed chemically or electrochemically by small-molecule mimics,[1,61,62,66] all-ferrous [4Fe−4S] clusters having biologically relevant terminal ligands have not been isolated. Recent XAS studies on Fd, HiPIP, and a [4Fe−4S] model complex revealed that the wide differences in redox windows of seemingly identical tetrairon cores arise from interactions between the first and second coordination spheres.[67] Specifically, hydrogen-bonding interactions extending to the bridging sulfido groups significantly reduce their covalent interaction with the iron centers, destabilizing higher oxidation states. The $\{Fe_4(\mu\text{-}OH)_4\}$ core in the compounds **1**−**3** can be formally regarded as a quadruply protonated, hypothetical $\{Fe_4(\mu\text{-}O)_4\}$ unit, an analogue of $\{Fe_4(\mu\text{-}S)_4\}$ with a lighter chalcogenide. By analogy to the sulfido-bridged core, such protonation of the bridging ligands greatly stabilizes low-valent metal centers, allowing isolation of all-ferrous tetrairon cubes **1**−**3**.

The existence of an oxo-bridged synthetic tetrairon(III) core[12] and the hydroxo-bridged tetrairon(II) complexes **1**−**3** allows one to envision hypothetical redox processes involving hydroxo/oxo-bridged cubane clusters. Iron oxyhydroxides and oxides are intermediates in the hydrolytic chemistry involved in the biomineralization of iron.[68] The nuclearity and coordination geometry of such clusters are controlled by various exogenous ligands including protein side chains that act as templates to direct the structure of the mineral phase.[11] With a proper arrangement of the proton donor/acceptor groups in the second coordination sphere, the [4Fe−4O(H)] unit may retain its structural integrity and act as an electron carrier for redox processes. It remains to be seen whether nature has chosen to construct a suitable platform to support such tetranuclear iron clusters for biological ET.

Acknowledgment. This work was supported by a grant from the National Science Foundation. A.C. and L.S. acknowledge the financial support of the Italian MURST and CNR and EC for Grant HPRN-CT-1999-0012 MOLNANOMAG. We thank Ms. Jane Kuzelka for her help in acquiring the Mössbauer spectra.

Supporting Information Available: Figure S1 showing the fully labeled ORTEP diagram of **2**, Figures S2 and S3 displaying solid-state structures of **1** and **3**, Figures S4−S6 showing the physical characterization of **1**−**3**, and an X-ray crystallographic file (CIF). This material is available free of charge via the Internet at http://pubs.acs.org.

IC010726B

(54) McNeese, T. J.; Mueller, T. E.; Wierda, D. A.; Darensbourg, D. J.; Delord, T. J. *Inorg. Chem.* **1985**, *24*, 3465−3468.
(55) Copp, S. B.; Holman, K. T.; Sangster, J. O. S.; Subramanian, S.; Zaworotko, M. J. *J. Chem. Soc., Dalton Trans.* **1995**, 2233−2243.
(56) He, C.; Lippard, S. J. *J. Am. Chem. Soc.* **2000**, *122*, 184−185.
(57) Aurivillius, B. *Acta Chem. Scand., Ser. A* **1977**, *31*, 501−508.
(58) Sletten, J.; Sørensen, A.; Julve, M.; Journaux, Y. *Inorg. Chem.* **1990**, *29*, 5054−5058.
(59) He, C.; Lippard, S. J. *Inorg. Chem.* **2001**, *40*, 1414−1420.
(60) Marcus, R. A.; Sutin, N. *Biochim. Biophys. Acta* **1985**, *811*, 265−322.
(61) O'Sullivan, T.; Millar, M. M. *J. Am. Chem. Soc.* **1985**, *107*, 4096−4097.
(62) Carney, M. J.; Papaefthymiou, G. C.; Frankel, R. B.; Holm, R. H. *Inorg. Chem.* **1989**, *28*, 1497−1503.
(63) Sigfridsson, E.; Olsson, M. H. M.; Ryde, U. *Inorg. Chem.* **2001**, *40*, 2509−2519.
(64) Yoo, S. J.; Angove, H. C.; Burgess, B. K.; Hendrich, M. P.; Münck, E. *J. Am. Chem. Soc.* **1999**, *121*, 2534−2545.
(65) Strop, P.; Takahara, P. M.; Chiu, H.-J.; Angove, H. C.; Burgess, B. K.; Rees, D. C. *Biochemistry* **2001**, *40*, 651−656.
(66) Goh, C.; Segal, B. M.; Huang, J.; Long, J. R.; Holm, R. H. *J. Am. Chem. Soc.* **1996**, *118*, 11844−11853.
(67) Glaser, T.; Bertini, I.; Moura, J. J. G.; Hedman, B.; Hodgson, K. O.; Solomon, E. I. *J. Am. Chem. Soc.* **2001**, *123*, 4859−4860.
(68) Theil, E. C.; Raymond, K. N. In *Bioinorganic Chemistry*; Bertini, E., Gray, H. B., Lippard, S. J., Valentine, J. S., Eds.; University Science Books: Mill Valley, CA, 1994; pp 1−35.